Thermochemical behavior and transport properties of Pr-substituted SrTiO$_3$ as potential solid oxide fuel cell anode

A.A. Yaremchenko*, S.G. Patrício, J.R. Frade

Department of Materials and Ceramic Engineering, CICECO, University of Aveiro, 3810-193 Aveiro, Portugal

HIGHLIGHTS

- Reduced and oxidized Sr$_{1-x}$Pr$_x$TiO$_{3\pm\delta}$ and Sr$_{1-1.5x}$Pr$_x$TiO$_{3\pm\delta}$ ($x = 0.02-0.30$) were synthesized.
- Pr substitutes in Sr sublattice in mixed 4+/3+ state and is insoluble in Ti sublattice.
- Reduction at high temperatures results in 2–3 orders increase of electrical conductivity.
- Very slow reduction kinetics is observed at temperatures below 1273 K.
- (Sr,Pr)TiO$_{3\pm\delta}$ show moderate thermal expansion and very small chemical expansion.

ARTICLE INFO

ABSTRACT

Phase composition, structural stability, electrical properties, thermochemical expansion and redox behavior of Pr-substituted SrTiO$_3$ were assessed for potential application in solid oxide fuel cell anodes. XRD analysis confirms formation of single-phase perovskite-like Sr$_{1-x}$Pr$_x$TiO$_{3\pm\delta}$ and Sr$_{1-1.5x}$Pr$_x$TiO$_{3\pm\delta}$ ($x = 0.02-0.30$) ceramics under both oxidizing and reducing conditions, although microstructural studies indicate minor precipitation of TiO$_2$ in reduced Sr-deficient ceramics with high Pr content. XPS analysis in combination with XRD suggests that Pr cations substitute into strontium sublattice in mixed 4+/3+ oxidation state and are essentially insoluble in titanium sublattice. Reduction at elevated temperatures results in 2–3 orders of magnitude increase of n-type electronic conductivity with respect to oxidized materials. Thermogravimetric and electrical studies demonstrate however very slow reduction kinetics at temperatures below 1273 K associated with nearly frozen equilibrium in cation sublattice and low oxygen vacancy concentration in oxidized materials. Electrical behavior is discussed in conjunction with defect chemistry of donor-doped strontium titanate. All oxidized and reduced materials exhibit moderate thermal expansion coefficients, compatible with that of common solid electrolytes, and a small contribution of chemical expansion on reduction.

© 2013 Elsevier B.V. All rights reserved.

1. Introduction

State-of-the-art nickel-based cermet anodes show excellent electrochemical performance in hydrogen-based fuels and are used in solid oxide fuel cell (SOFC) prototypes for several decades. They suffer however from large dimensional changes in inevitable redox cycles leading to degradation of microstructure and performance [1]. These cermets are also prone to coking and sulfur poisoning in hydrocarbon fuels resulting in blocking and loss of performance of porous anodes [2,3]. Significant efforts are aimed therefore on the search for alternative anode materials exhibiting phase stability

and high electrical conductivity under fuel conditions, sufficient electrochemical activity, and chemical and thermomechanical compatibility with solid electrolytes. In particular, perovskite-like materials with electronic or mixed ionic-electronic conductivity are considered as possible substitutes to nickel in SOFC anodes. Representative examples are (La,Sr)(Cr,Mn)O$_{3-\delta}$, Sr$_2$MgMoO$_{6-\delta}$, donor-doped SrTiO$_3$ and SrVO$_{3-\delta}$-based materials [3,4].

Donor-doped SrTiO$_3$ ceramics are known to exhibit phase stability under both oxidizing and reducing conditions. High electrical conductivity can be obtained by reduction at high temperatures [3–5]. Furthermore, strontium titanate derivatives exhibit moderate thermal expansion [5], do not catalyze carbon deposition [6] and are tolerant with respect to H$_2$S [7,8]. SrTiO$_3$ ceramics with additions of lanthanum [8–11] or yttrium [7,12–14] into strontium sublattice or niobium [14–18] into titanium sublattice were

* Corresponding author. Tel.: +351 234 370235; fax: +351 234 370204.
E-mail address: ayaremchenko@ua.pt (A.A. Yaremchenko).

characterized for possible use in SOFC anodes. Although defect chemistry of donor-doped $SrTiO_3$ is not completely established, it is generally accepted that charge compensation for donor additions may be different under oxidizing and reducing conditions, and also depends on the A:B site ratio [18–20]. However, reversibility between oxidizing and strongly reducing conditions is arguable at temperatures characteristic for SOFC operation. Furthermore, significant scattering in reported conductivity values for reduced $SrTiO_3$-based materials suggest that the electronic conductivity is strongly affected by thermal pre-history [3,14].

The present work was focused on appraisal of Pr-substituted $SrTiO_3$ for possible application as SOFC anode component. $Sr_{1-x}Pr_xTiO_3$ has previously attracted some attention due to room-temperature ferroelectricity induced by praseodymium doping (e.g. Refs. [21,22]); in this connection, several reports on structural characterization were published for moderate Pr contents ($x \leq 0.30$) [22–26]. Contrary to La-, Y- and Nb-containing systems, praseodymium cations may substitute in a mixed $4+/3+$ oxidation state [21] and, thus, may be expected to contribute to the electro-catalytic properties. For instance, $PrMnO_3$-based cathodes were reported to exhibit a superior electrochemical performance compared to the analogs based on the other lanthanides [27]. Infiltration of praseodymia into porous cathodes is also a well-established technique to enhance the surface exchange kinetics and electrocatalytic activity [27]. In the present work, three series of ceramic materials were prepared including $Sr_{1-x}Pr_xTiO_{3\pm\delta}$ with nominal stoichiometric A:B site ratio, nominally A-site deficient $Sr_{1-1.5x}Pr_xTiO_{3\pm\delta}$, and nominally B-site substituted $SrTi_{1-y}Pr_yO_{3\pm\delta}$. The latter series were synthesized in order to assess the possible incorporation of Pr cations into titanium sites. The attention was focused on the properties relevant for SOFC application, including phase relationships and structural stability under different conditions, electrical transport properties, thermochemical expansion and its compatibility with solid electrolytes, and dimensional stability in redox cycles. The average Pr oxidation state was determined by X-ray photoelectron spectroscopy (XPS). As anode layers in SOFC-type solid electrolyte cells are conventionally fabricated in air with subsequent in-situ reduction, special attention was given to possibility of reduction of Pr-substituted $SrTiO_3$ at temperatures characteristic for SOFC operation.

2. Experimental

Powders of samples with nominal cation stoichiometry $Sr_{1-x}Pr_xTiO_{3\pm\delta}$ ($x = 0.02, 0.05, 0.10, 0.20$ and 0.30), "A-site deficient" $Sr_{1-1.5x}Pr_xTiO_{3\pm\delta}$ ($x = 0.02, 0.05, 0.10, 0.20$ and 0.30), and "B-site substituted" $SrTi_{1-y}Pr_yO_{3\pm\delta}$ ($y = 0.02, 0.05$ and 0.10) were prepared by conventional solid state route using $SrCO_3$ (Sigma–Aldrich, $\geq$99.9%), TiO_2 (Sigma–Aldrich, 99.8%) and Pr_6O_{11} (Sigma–Aldrich, 99.9%). Prior to weighing, titanium oxide was dried at 973 K for 2 h in air. The precursor mixtures were calcined consecutively at 1173, 1373, 1473 and 1523 K for 5 h at each temperature, with intermediate regrindings, to attain high homogeneity. After subsequent ball-milling with ethanol, disk-shaped ceramic samples were compacted uniaxially and sintered in air or $10\%H_2-N_2$ atmospheres. Sintering conditions for A-site substituted materials are listed in Table 1. In case of $SrTi_{1-y}Pr_yO_{3\pm\delta}$, sintering was performed for 10 h in air at 2023 K for $y = 0.02$ and 1973 K for $y = 0.05-0.10$. As substitution with praseodymium generally improves the sinter-ability (see below), the sintering temperature was gradually decreased with Pr content for all series. For $Sr_{0.98}Pr_{0.02}TiO_{3\pm\delta}$, $Sr_{0.95}Pr_{0.05}TiO_{3\pm\delta}$ and $Sr_{0.97}Pr_{0.02}TiO_{3\pm\delta}$ compositions, the upper temperature limit of available equipment for sintering under reducing conditions ($\approx$1773 K) was rather insufficient to prepare ceramics samples with reasonable densities. Therefore, these

Table 1
Sintering conditions and properties of (Sr,Pr)TiO$_3$ ceramics.

Composition	Sintering	Grain size, μm	Density, g cm^{-3}	Relative density, %
Oxidized ceramics				
$Sr_{0.98}Pr_{0.02}TiO_{3\pm\delta}$	Air/2023 K/10 h	2–7	4.95	96.4
$Sr_{0.95}Pr_{0.05}TiO_{3\pm\delta}$	Air/1973 K/10 h	2–11	4.83	93.3
$Sr_{0.90}Pr_{0.10}TiO_{3\pm\delta}$	Air/1973 K/10 h	3–14	5.02	95.3
$Sr_{0.80}Pr_{0.20}TiO_{3\pm\delta}$	Air/1923 K/10 h	6–18	4.81	88.8
$Sr_{0.70}Pr_{0.30}TiO_{3\pm\delta}$	Air/1923 K/10 h	5–15	4.73	85.1
$Sr_{0.97}Pr_{0.02}TiO_{3\pm\delta}$	Air/2023 K/10 h	5–11	4.86	95.0
$Sr_{0.925}Pr_{0.05}TiO_{3\pm\delta}$	Air/1973 K/10 h	4–13	4.91	95.8
$Sr_{0.85}Pr_{0.10}TiO_{3\pm\delta}$	Air/1973 K/10 h	4–30	4.84	94.0
$Sr_{0.70}Pr_{0.20}TiO_{3\pm\delta}$	Air/1923 K/10 h	11–66	4.90	94.0
$Sr_{0.55}Pr_{0.30}TiO_{3\pm\delta}$	Air/1873 K/10 h	16–71	4.58	87.1
Reduced ceramics				
$Sr_{0.98}Pr_{0.02}TiO_{3\pm\delta}$	Air/2023 K/10 h + 10%H$_2$/1773 K/10 h	1.5–6	4.91	95.5
$Sr_{0.95}Pr_{0.05}TiO_{3\pm\delta}$	Air/1973 K/10 h + 10%H$_2$/1773 K/10 h	3–13	4.85	93.7
$Sr_{0.90}Pr_{0.10}TiO_{3\pm\delta}$	10%H$_2$/1773 K/10 h	0.7–6	5.15	98.0
$Sr_{0.80}Pr_{0.20}TiO_{3\pm\delta}$	10%H$_2$/1773 K/10 h	1.5–7	4.14	76.6
$Sr_{0.70}Pr_{0.30}TiO_{3\pm\delta}$	10%H$_2$/1773 K/10 h	1–5	3.69	66.4
$Sr_{0.97}Pr_{0.02}TiO_{3\pm\delta}$	Air/2023 K/10 h + 10%H$_2$/1773 K/10 h	3–15	4.85	95.0
$Sr_{0.925}Pr_{0.05}TiO_{3\pm\delta}$	10%H$_2$/1773 K/10 h	1–6	4.86	94.8
$Sr_{0.85}Pr_{0.10}TiO_{3\pm\delta}$	10%H$_2$/1773 K/10 h	4–32	4.99	97.1
$Sr_{0.70}Pr_{0.20}TiO_{3\pm\delta}$	10%H$_2$/1773 K/10 h	2–26	4.91	94.7
$Sr_{0.55}Pr_{0.30}TiO_{3\pm\delta}$	10%H$_2$/1673 K/10 h	3–22	4.68	89.4
Porous oxidized samples				
$Sr_{0.90}Pr_{0.10}TiO_{3\pm\delta}$	Air/1673 K/10 h		3.32	62.9
$Sr_{0.80}Pr_{0.20}TiO_{3\pm\delta}$	Air/1673 K/10 h		3.07	56.7
$Sr_{0.85}Pr_{0.10}TiO_{3\pm\delta}$	Air/1573 K/10 h		3.94	76.5
$Sr_{0.70}Pr_{0.20}TiO_{3\pm\delta}$	Air/1543 K/10 h		4.30	82.5

Note: relative density was estimated neglecting oxygen nonstoichiometry.

samples were preliminary sintered in air and then reduced at 1773 K for 10 h in reducing atmosphere (Table 1). In the course of sintering/annealing, Pt foil or a thick layer of the powder with the same compositions were used as substrates in air and hydrogen-based atmospheres, respectively, to avoid reaction with alumina supports.

For preparation of porous ceramics, the powders underwent several additional calcination steps, with maximum temperatures of 1623 K for $x = 0.10$ and 1673 K for $x = 0.20$, with subsequent ball-milling. Porous ceramic samples were compacted and sintered under appropriate conditions (Table 1).

Dense ceramic samples of $Ce_{0.9}Gd_{0.1}O_{2-\delta}$ (CGO) and $(La_{0.9}Sr_{0.1})_{0.98}Ga_{0.8}Mg_{0.2}O_{3-\delta}$ (LSGM) solid electrolytes for comparative dilatometric measurements were prepared using commercial powders and sintered in air (CGO: Rhodia Specialty Chemicals, 1873 K/5 h; LSGM: Praxair Specialty Ceramics, 1673 K/4 h).

The obtained dense and porous disk samples were cut into rectangular bars for electrical and dilatometric measurements. The density of prepared ceramics was calculated from the geometric dimensions and mass of polished samples. For X-ray diffraction (XRD) and thermogravimetric measurements, dense ceramic samples were ground to powders in a mortar.

XRD patterns were recorded at room temperature using a Rigaku D/Max-B diffractometer (CuK$_\alpha$, $2\Theta = 10-80°$, step 0.02°, exposition 3 s). Unit cell parameters were calculated from the XRD data using Fullprof software (profile matching method). Micro-structural characterization was performed by scanning electron microscopy (SEM, Hitachi S-4100 and SU-70 instruments) coupled with energy dispersive spectroscopy (EDS, Rontec UHV and Bruker Quantax 400 detectors, respectively). Dilatometric measurements (vertical Linseis L75V/1250 instrument) and thermogravimetric analysis (TGA, Setaram SetSys 16/18 instrument) were carried out in flowing air, argon or $10\%H_2-N_2$ mixture at $298-1373$ K with

constant heating/cooling rate of 2–3 K min^{-1} or isothermally as function of time. Electrical conductivity was measured using impedance spectroscopy (Agilent 4284A precision LCR meter) and 4-probe DC technique as function of temperature in controlled atmospheres, as function of oxygen partial pressure under reducing conditions using H$_2$–H$_2$O–N$_2$ mixtures, or isothermally in variable atmospheres. The Seebeck coefficient in air was determined at 773–1273 K and temperature difference 20–30 K; the values were corrected for thermopower of Pt leads. In all cases (synthesis and measurements), oxygen partial pressure $p(O_2)$ in gas atmosphere was monitored using yttria-stabilized zirconia (YSZ) solid-electrolyte sensor; $p(O_2)$ in 10%H$_2$–N$_2$ flow corresponded to ∼10^{-19} atm at 1173 K.

X-ray photoelectron spectroscopy (XPS) studies were performed at CEMUP (University of Porto, Portugal) on the surface of as-polished samples using a VG Scientific ESCALAB 200A spectrometer with a non-monochromatized Al Kα radiation (1486.6 eV) operated at 300 W. The measurements were carried out with a take-off angle of 90° at room temperature. Survey spectra were collected with the pass energy of 50 eV, while 20 eV were used for Ti 3p and Pr 3d core-level regions. Deconvolution of high-resolution spectra was done using XPSPEAK41 software with symmetric Gaussian–Lorentzian line shape, Shirley-type background subtraction, and nonlinear least-square procedure for peak fitting. Peak intensities of Ti 2p and Pr 3d spin–split doublets were estimated taking into account Scofield's photoionization cross-section values [28]. Praseodymium cations fractions were estimated from the corresponding peak areas using sensitivity factors provided by instrument manufacture, with a standard accuracy of ±10%. The C 1s band (from adventitious carbon) at 285.0 eV was used as an internal standard to correct possible deviations caused by charging of the samples surface. The accuracy of core-level binding energy values was ±0.2 eV. Pr$_6$O$_{11}$ (Sigma–Aldrich, 99.9%) and Pr$_2$O$_3$ (Alfa Aesar, 99.9%) were also analyzed as reference materials.

3. Results and discussion

3.1. Phase composition, structure and microstructure

XRD analysis showed, in addition to the main perovskite phase, the presence of secondary phases for all sintered ceramics with nominal composition SrTi$_{1-y}$Pr$_y$O$_{3\pm\delta}$. The impurity phases included Ruddlesden–Popper Sr$_{n+1}$Ti$_n$O$_{3n+1}$ for $y = 0.02$–0.10 and PrO$_{2-\delta}$ for $y = 0.05$–0.10 (Fig. 1A and B). These results indicate that praseodymium cations do not substitute into titanium sublattice (at least, under oxidizing conditions), in agreement with recent report on XRD and EXAFS analysis of SrTi$_{0.95}$Pr$_{0.05}$O$_3$ [25].

No evidence of secondary phases was observed on XRD patterns of sintered A-site substituted materials. Both series of "cation-stoichiometric" Sr$_{1-x}$Pr$_x$TiO$_{3\pm\delta}$ and "A-site deficient" Sr$_{1-1.5x}$Pr$_x$TiO$_{3\pm\delta}$, prepared either under oxidizing or reducing conditions, were apparently single-phase perovskites (Fig. 1C − F). At the same time, microstructural analysis (SEM/EDS) of Sr$_{0.70}$Pr$_{0.20}$TiO$_{3\pm\delta}$ and Sr$_{0.55}$Pr$_{0.20}$TiO$_{3\pm\delta}$ ceramics showed traces of secondary phase at the grain boundary. The amount of this phase was negligible for oxidized materials, but increases upon reduction and with Pr content in reduced samples. Still, the amount of segregated phase was too small to be detected by XRD. EDS analysis revealed that precipitated impurity grains are Sr-free and Ti-rich, and can be therefore identified as TiO$_2$ or Magneli Ti$_n$O$_{2n-1}$ phases.

The crystal structure of materials with small praseodymium content ($x < 0.10$) was identified as cubic (space group $Pm\bar{3}m$) (Table 2), similar to parent SrTiO$_3$ at room temperature. Increasing Pr concentration resulted in reducing lattice symmetry to tetragonal, in agreement with the previous reports [23–25]. This was
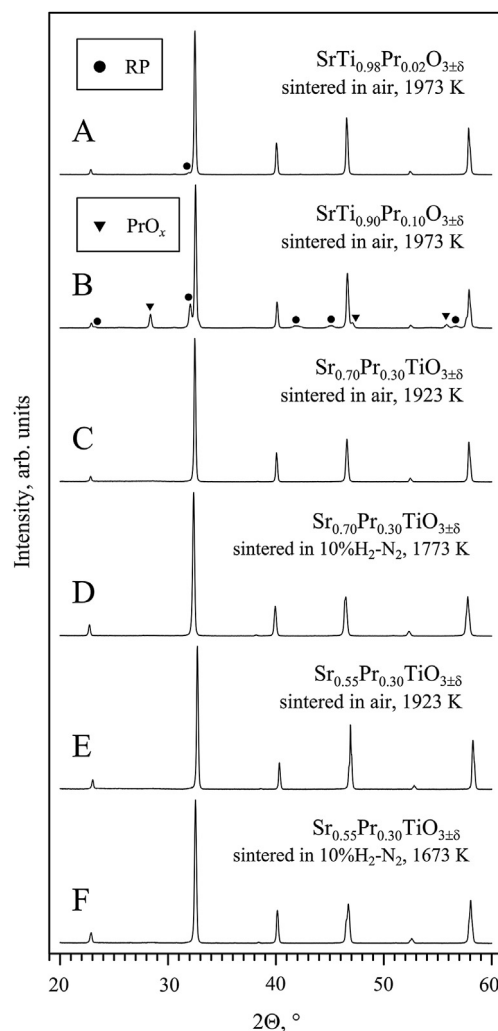

Fig. 1. XRD patterns of Pr-substituted SrTiO$_3$ samples sintered in different atmospheres.

evidenced, in particular, by appearance of small additional peaks at $2\Theta \sim 38.2$–38.4° and 50.9–51.1°, indexed as 211 and 213 reflections, respectively, and splitting of peaks at $2\Theta \sim 76.9$–77.7°. It was assumed [24,25] that substitution with praseodymium increases temperature of tetragonal-cubic structural transition, characteristic for undoped SrTiO$_3$ at 105–110 K (e.g. Refs. [29,30]). Tetragonal distortion of (Sr,Pr)TiO$_3$ perovskite lattice was explained by tilting of oxygen octahedra as a result of incorporation of smaller Pr cations into Sr sites [24]. In present work, the transition from cubic to tetragonal symmetry was found to occur at $x \sim 0.10$. XRD patterns of tetragonal perovskites were refined using $I4/mcm$ space group (Table 2) suggested earlier in Ref. [24] and characteristic for tetragonal SrTiO$_3$. For reduced Sr$_{0.70}$Pr$_{0.30}$TiO$_{3\pm\delta}$, additional splitting of higher-angle reflection indicated further decrease of lattice symmetry. XRD pattern of this material was successfully refined using orthorhombic space group $Imma$ (Table 2) suggested previously for Sr$_{0.7}$La$_{0.3}$TiO$_{3\pm\delta}$ [31].

Calculated lattice parameters and pseudocubic cell volumes are listed in Table 2. For Sr$_{1-x}$Pr$_x$TiO$_{3\pm\delta}$ series, no evident correlation between substitution level and unit cell volume was observed. This can be explained, most likely, by complex defect formation and charge compensation mechanism (as discussed below) affecting the lattice dimensional parameters. On the contrary, substitution of smaller Pr^{3+}/Pr^{4+} cations into strontium sublattice of

Table 2
Structural parameters of $(Sr,Pr)TiO_{3\pm\delta}$ perovskites.

| Composition	Lattice	Space group	Unit cell parameters			
			a, Å	b, Å	c, Å	V, Å³ [a]
Oxidized ceramics						
$Sr_{0.98}Pr_{0.02}TiO_{3\pm\delta}$	Cubic	$Pm\overline{3}m$	3.9080 (2)			59.68
$Sr_{0.95}Pr_{0.05}TiO_{3\pm\delta}$	Cubic	$Pm\overline{3}m$	3.9083 (2)			59.70
$Sr_{0.90}Pr_{0.10}TiO_{3\pm\delta}$	Tetragonal	$I4/mcm$	5.5226 (3)		7.8133 (5)	59.57
$Sr_{0.80}Pr_{0.20}TiO_{3\pm\delta}$	Tetragonal	$I4/mcm$	5.5202 (1)		7.8212 (2)	59.58
$Sr_{0.70}Pr_{0.30}TiO_{3\pm\delta}$	Tetragonal	$I4/mcm$	5.5211 (2)		7.8225 (3)	59.61
$Sr_{0.97}Pr_{0.02}TiO_{3\pm\delta}$	Cubic	$Pm\overline{3}m$	3.9066 (1)			59.62
$Sr_{0.925}Pr_{0.05}TiO_{3\pm\delta}$	Cubic	$Pm\overline{3}m$	3.9060 (2)			59.59
$Sr_{0.85}Pr_{0.10}TiO_{3\pm\delta}$	Cubic	$Pm\overline{3}m$	3.9024 (2)			59.43
$Sr_{0.70}Pr_{0.20}TiO_{3\pm\delta}$	Tetragonal	$I4/mcm$	5.5035 (2)		7.7984 (3)	59.05
$Sr_{0.55}Pr_{0.30}TiO_{3\pm\delta}$	Tetragonal	$I4/mcm$	5.4939 (2)		7.7921 (3)	58.80
Reduced ceramics						
$Sr_{0.98}Pr_{0.02}TiO_{3\pm\delta}$	Cubic	$Pm\overline{3}m$	3.9076 (3)			59.67
$Sr_{0.95}Pr_{0.05}TiO_{3\pm\delta}$	Cubic	$Pm\overline{3}m$	3.9086 (3)			59.71
$Sr_{0.90}Pr_{0.10}TiO_{3\pm\delta}$	Tetragonal	$I4/mcm$	5.5207 (3)		7.8202 (5)	59.59
$Sr_{0.80}Pr_{0.20}TiO_{3\pm\delta}$	Tetragonal	$I4/mcm$	5.5190 (3)		7.8363 (4)	59.67
$Sr_{0.70}Pr_{0.30}TiO_{3\pm\delta}$	Orthorhombic	$Imma$	5.5378 (2)	7.7971 (3)	5.5217 (2)	59.61
$Sr_{0.97}Pr_{0.02}TiO_{3\pm\delta}$	Cubic	$Pm\overline{3}m$	3.9082 (2)			59.69
$Sr_{0.925}Pr_{0.05}TiO_{3\pm\delta}$	Cubic	$Pm\overline{3}m$	3.9056 (2)			59.58
$Sr_{0.85}Pr_{0.10}TiO_{3\pm\delta}$	Tetragonal	$I4/mcm$	5.5179 (7)		7.8140 (9)	59.48
$Sr_{0.70}Pr_{0.20}TiO_{3\pm\delta}$	Tetragonal	$I4/mcm$	5.5108 (3)		7.8250 (4)	59.41
$Sr_{0.55}Pr_{0.30}TiO_{3\pm\delta}$	Tetragonal	$I4/mcm$	5.5002 (2)		7.8122 (3)	59.09

[a] Pseudocubic cell volume.

$Sr_{1-1.5x}Pr_xTiO_{3\pm\delta}$ results in progressive contraction of perovskite lattice.

Phase evolution during the solid state synthesis of $(Sr,Pr)TiO_{3\pm\delta}$ was monitored on powders for preparation of porous ceramic samples. For instance, XRD analysis of $Sr_{0.85}Pr_{0.10}TiO_{3\pm\delta}$ powder showed the presence of TiO_2, $Sr_3Ti_2O_7$, Pr_6O_{11} and $PrO_{2-\delta}$ phase impurities after calcination at 1250C, only traces of TiO_2 and $Pr_2Ti_2O_7$ after treatments at 1300C, and single-phase perovskite after final annealing at 1350C. Similar sequences were

characteristic for other compositions, although slightly higher calcination temperature was required for materials with larger Pr content. All porous ceramic samples with $x = 0.10$ and 0.20 were found single-phase after final sintering.

Typical microstructures of prepared ceramic materials are illustrated in Fig. 2(A and B). Increasing praseodymium content and introduction of cation vacancies were found to promote strongly the grain growth during sintering. In order to prevent possible onset of liquid phase, the sintering temperature in air was gradually
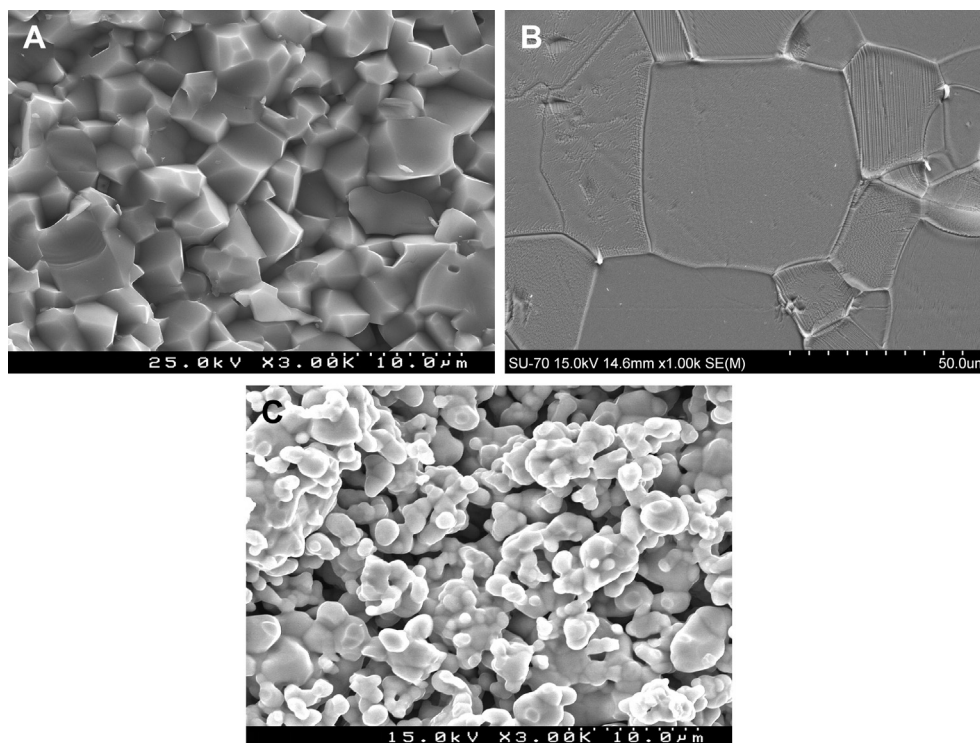
Fig. 2. SEM micrographs of (A) fractured $Sr_{0.98}Pr_{0.02}TiO_{3\pm\delta}$ ceramics sintered in air at 2023 K; (B) polished and thermally etched $Sr_{0.70}Pr_{0.20}TiO_{3\pm\delta}$ ceramics sintered in air at 1923 K; (C) fractured porous $Sr_{0.80}Pr_{0.20}TiO_{3\pm\delta}$ ceramics sintered in air at 1673 K.

decreased with x. Even with this precaution, the grain size of air-sintered samples increased from 2–7 µm for $Sr_{0.98}Pr_{0.02}TiO_{3\pm\delta}$ to 10–70 µm for $Sr_{1-1.5x}Pr_xTiO_{3\pm\delta}$ ($x = 0.20-0.30$) (Table 1 and Fig. 2A and B). For almost all oxidized samples the relative density was ∼90% and higher. Similar results were obtained during the sintering in hydrogen-based atmosphere, although the grain sizes of reduced ceramics were smaller due to lower-temperature processing. $Sr_{0.80}Pr_{0.20}TiO_{3\pm\delta}$ and $Sr_{0.70}Pr_{0.30}TiO_{3\pm\delta}$ samples show relatively low density and open porosity due to rather insufficient sintering temperature (a limitation of available equipment). One example of microstructure of prepared porous ceramic samples is given in Fig. 2C. Similar to the dense ceramics, the relative density of porous samples was higher for cation-deficient compositions, even after sintering at rather low temperature, increasing from ∼60% for $Sr_{1-x}Pr_xTiO_{3\pm\delta}$ to ∼80% for $Sr_{1-1.5x}Pr_xTiO_{3\pm\delta}$ (Table 1).

3.2. XPS spectra

In order to evaluate the oxidation state of praseodymium cations in $(Sr,Pr)TiO_{3\pm\delta}$, XPS spectra of selected ceramic samples were recorded and analyzed by comparing to spectra obtained for praseodymium oxides, Pr_6O_{11} and Pr_2O_3, as reference materials. Core-level binding energies (BEs) obtained by curve-fitting the XPS spectra are summarized in Table 3.

The obtained XPS spectra of Pr_2O_3 and Pr_6O_{11} oxides (Fig. 3A and B) were quite similar to those reported in literature [32–37]. The deconvoluted high-resolution Pr 3d spectrum of Pr_6O_{11} (Fig. 3A) comprised two intense peaks at 933.7 (a') and 954.1 eV (b') corresponding to $3d_{5/2}$ and $3d_{3/2}$ core-levels, respectively, with a splitting energy of ∼20 eV, in agreement with literature data [35,36]. Two additional spin–split doublets were observed at 929.4/949.8 eV (a/b) and at 945.9/966.3 eV (a''/b''). The spectrum of Pr_6O_{11} (Fig. 3A) comprises also a satellite peak (labeled t) located ∼957.6 eV and associated with multiplet effect [36,37], and oxygen Auger peak at ∼971.5 eV. It should be pointed out that a/b and a'/b' doublets are typical contribution of both Pr_2O_3 and Pr_6O_{11} spectra and thus cannot be directly assigned to specific oxidation states of praseodymium. The only unique assignment to a specific oxidation state can be done for a''/b'' doublet (ascribed to $3d^9 4f^1$ configuration) which is completely absent in Pr 3d spectra of pure Pr_2O_3 (Fig. 3B and Ref. [37]) being a fingerprint of Pr^{4+}. Typical features of Pr_2O_3 spectrum (Fig. 3B) include the appearance of an additional shoulder at 944.2 eV (labeled m; another multiplet effect-related satellite) and shift of oxygen Auger peak to higher BE.

Fig. 4 illustrates typical Ti 2p and Pr 3d spectra of $(Sr,Pr)TiO_{3\pm\delta}$ ceramic samples. Ti 2p XPS spectra of reduced ceramics (Fig. 4A) were quite similar to those of the samples sintered in air and showed two symmetric peaks at 458.4 eV (Ti $2p_{3/2}$) and 464.1 eV (Ti $2p_{1/2}$) characteristic of Ti^{4+} state [38]. No shoulders at a lower
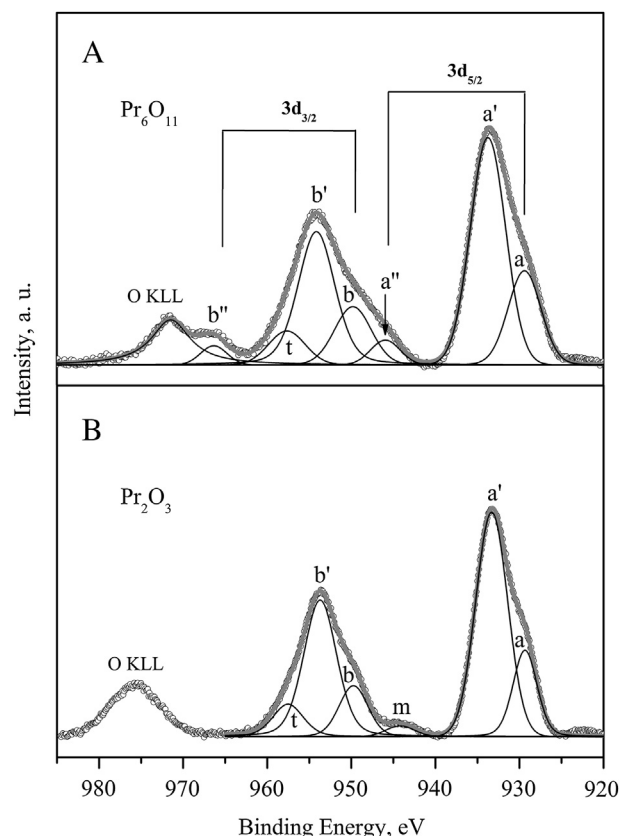

Fig. 3. Pr 3d deconvoluted high-resolution XPS spectra of (A) Pr_6O_{11} and (B) Pr_2O_3. The overall simulated spectra are represented by gray lines.

binding energy typically assigned to Ti^{3+} were detected, thus indicating that the concentration of titanium cations in 3+ oxidation state was below the XPS detection limits under given experimental conditions even in reduced samples.

Pr 3d spectra of oxidized $(Sr,Pr)TiO_{3\pm\delta}$ samples (Fig. 4B) exhibited $3d_{5/2}$ and $3d_{3/2}$ band peaks with BEs similar to those for Pr_6O_{11} (Table 3). At the same time, a decrease in relative intensity of a'' peak associated with 4+ oxidation state indicated a decrease of relative Pr^{4+} surface content compared to reference Pr_6O_{11} oxide. The area of the b'' peak could not be resolved due to overlapping with strong oxygen Auger peak. Besides that, the appearance of additional shoulder m at ∼444 eV characteristic for Pr_2O_3 also supports the presence of larger fraction of Pr^{3+} in $(Sr,Pr)TiO_{3\pm\delta}$. Pr 3d profiles of reduced $(Sr,Pr)TiO_{3\pm\delta}$ samples showed no significant alterations compared to oxidized materials, thus suggesting similar

Table 3
Binding energies for Pr 3d core-level photoemission spectra of Pr_6O_{11}, Pr_2O_3 and $(Sr,Pr)TiO_{3\pm\delta}$.

Sample	Binding energy, eV[a]							
	a	a'	m	a''	b	b'	t	b''
Pr_6O_{11}	929.4 (4.60)	933.7 (4.92)	–	945.9 (4.13)	949.8 (5.13)	954.1 (5.17)	957.6 (5.14)	966.3 (3.70)[b]
Pr_2O_3	929.3 (3.37)	933.3 (4.47)	944.2 (3.97)	–	949.7 (4.02)	953.7 (4.62)	957.5 (4.27)	–
$Sr_{0.85}Pr_{0.10}TiO_{3\pm\delta}$ (oxidized)	929.1 (3.73)	933.3 (3.85)	943.1 (3.98)	946.2 (3.69)	949.5 (4.14)	953.7 (3.91)	957.5 (1.84)	n/a[c]
$Sr_{0.85}Pr_{0.10}TiO_{3\pm\delta}$ (reduced)	929.6 (3.87)	933.7 (3.75)	944.1 (4.70)	946.8 (3.90)	950.0 (3.99)	954.1 (4.24)	958.2 (2.45)	n/a[c]
$Sr_{0.80}Pr_{0.20}TiO_{3\pm\delta}$ (oxidized)	929.0 (3.59)	933.2 (3.85)	943.5 (4.10)	946.2 (3.90)	949.4 (3.85)	953.6 (4.12)	957.6 (2.74)	n/a[c]
$Sr_{0.80}Pr_{0.20}TiO_{3\pm\delta}$ (reduced)	929.1 (3.75)	933.4 (3.79)	943.8 (4.50)	946.2 (3.80)	949.5 (4.04)	953.7 (4.12)	957.7 (2.53)	n/a[c]
$Sr_{0.70}Pr_{0.20}TiO_{3\pm\delta}$ (oxidized)	929.1 (3.96)	933.3 (3.81)	943.5 (4.00)	946.6 (3.76)	949.5 (4.30)	953.7 (3.88)	957.6 (2.90)	n/a[c]
$Sr_{0.70}Pr_{0.20}TiO_{3\pm\delta}$ (reduced)	929.5 (3.73)	933.7 (3.84)	944.7 (4.87)	946.7 (3.60)	949.9 (3.83)	954.1 (4.18)	958.0 (2.39)	n/a[c]

[a] Values in parentheses correspond to the FWHM (full-width at half maximum) of the bands obtained by spectra fitting.
[b] Estimated by modulation of the oxygen Auger peak.
[c] Not determined due to overlapping between Pr $3d_{3/2}$ and oxygen Auger peaks.
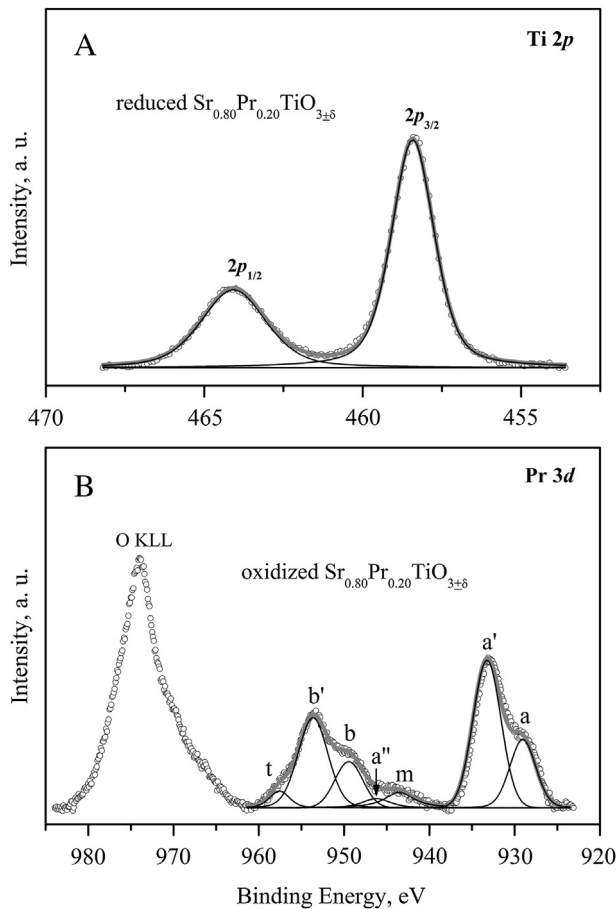
Fig. 4. Typical deconvoluted high-resolution XPS spectra: (A) Ti 2p core-level region for reduced $Sr_{0.80}Pr_{0.20}TiO_{3\pm\delta}$ and (B) Pr 3d core-level region for oxidized $Sr_{0.80}Pr_{0.20}TiO_{3\pm\delta}$. The overall simulated spectra are represented by gray lines.

Pr^{3+} and Pr^{4+} surface fractions. A slight shift of Pr 3d peaks to higher BEs values for reduced materials (Table 3) indicate a change in the praseodymium chemical environment, probably, due to minor structural differences.

Surface fractions of Pr^{3+} and Pr^{4+} cations in $(Sr,Pr)TiO_{3\pm\delta}$ ceramics were estimated using the method proposed by Borchert et al. [39]. This approximation method is based on the assumption that the ratio of a'' and a' peaks area exhibit a linear dependence on the relative Pr^{3+} content. The fraction of Pr^{3+} cations was estimated using the relation [39]:

$$\frac{[Pr^{3+}]}{[Pr^{3+}] + [Pr^{4+}]} = 1 - \frac{1}{c} \times \frac{area(a'')}{area(a')} \qquad (1)$$

The constant c was calculated from the XPS data for Pr_6O_{11} sample (with known Pr^{3+} fraction of ∼33%) to be equal to ∼0.14 under applied experimental conditions. Thus, since the peak a'' occurs only for Pr^{4+} cations, a''/a' peaks area ratio should be equal to zero when all praseodymium cations are in 3+ oxidation state (as in Pr_2O_3), whereas value of 0.14 is expected when all Pr cations are fully oxidized (e.g. for pure stoichiometric PrO_2 oxide).

The fractions of Pr^{4+} cations in selected $(Sr,Pr)TiO_{3\pm\delta}$ ceramic materials were estimated using Eq. (1) and are listed in Table 4. Taking into account the accuracy of XPS quantification, praseodymium cations substitute into strontium sublattice of $SrTiO_3$ with ratio $[Pr^{4+}]/[Pr^{3+}] \sim 1:1$. The fraction of Pr^{4+} cations in oxidized samples has a tendency to decrease with increasing total praseodymium content and with introduction of cation vacancies.

Table 4
Relative Pr^{4+} content in $(Sr,Pr)TiO_{3\pm\delta}$ ceramics estimated from the XPS data.

Composition	$[Pr^{4+}]/[Pr]^{total}$, %	
	Oxidized	Reduced
$Sr_{0.85}Pr_{0.10}TiO_{3\pm\delta}$	55	54
$Sr_{0.80}Pr_{0.20}TiO_{3\pm\delta}$	57	47
$Sr_{0.70}Pr_{0.20}TiO_{3\pm\delta}$	49	40

Nevertheless, the presence of Pr cation in 4+ oxidation state indicates that all oxidized samples are apparently oxygen overstoichiometric. The reduction leads to a reasonable decrease of average praseodymium oxidation state; still, significant fraction of Pr^{4+} is observed even in reduced samples. Very similar fractional changes of $Pr^{4+/3+}$ were obtained previously for oxidized and reduced $Ce_{1-x}Pr_xO_{2-\delta}$ ($x = 0.2, 0.4$) fluorites from the XPS data [39]. Duran et al. reported earlier $[Pr^{3+}]/[Pr^{4+}] \sim 2:1$ ratio for oxidized $Sr_{1-x}Pr_xTiO_3$ ($x = 0.025-0.075$) ceramics [21], however, the analysis of XPS spectra in that report seems oversimplified. Note that the presence of Pr cations in mixed 4+/3+ oxidation state was suggested also from the analysis of dielectric relaxation processes in $(Sr,Pr)TiO_3$ [26].

3.3. Defect chemistry and electrical properties of oxidized materials

All oxidized ceramics showed semiconducting behavior of electrical conductivity in air (Fig. 5). Seebeck coefficient values were in the range $-(390 \div 600)$ μV K^{-1} at 823–1223 K; the negative
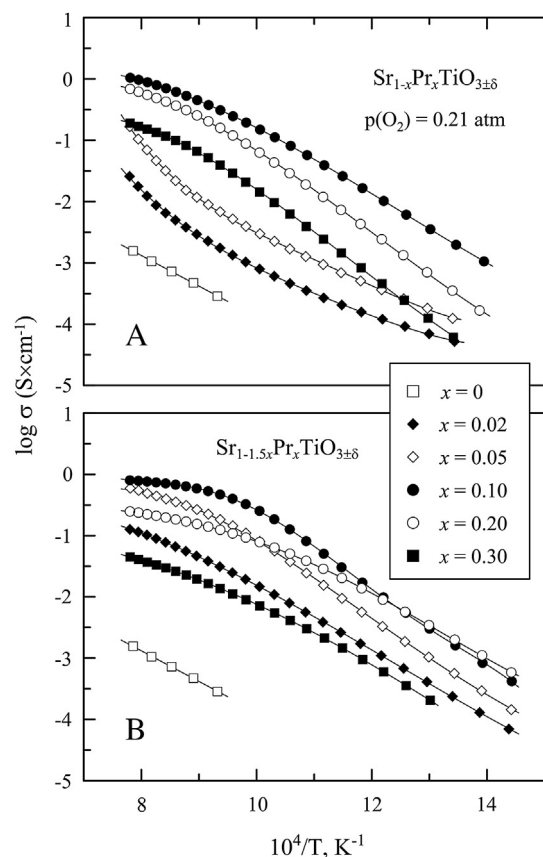
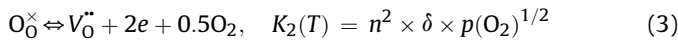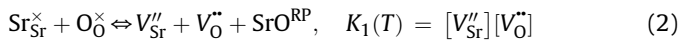**Fig. 5.** Temperature dependencies of electrical conductivity of (A) $Sr_{1-x}Pr_xTiO_{3\pm\delta}$ and (B) $Sr_{1-1.5x}Pr_xTiO_{3\pm\delta}$ ceramics in air. Literature data on undoped $SrTiO_3$ [40] are shown for comparison.

sign indicates that electronic conductivity is n-type. Ionic contribution to the total conductivity can be neglected [19]. For both series of ceramics, electronic transport increases with moderate praseodymium substitution (Fig. 6) and reaches the maximum at $x \sim 0.10-0.15$; slow decrease of conductivity is observed on further substitution.

The behavior of electrical properties can be considered taking into account the defect chemistry of donor-doped strontium titanate [18,19]. Since reduction of titanium cations to Ti^{3+} is unlikely under oxidizing conditions and interstitial oxygen anions cannot be accommodated in the perovskite structure, charge compensation in donor-doped $SrTiO_3$ should occur via formation of cation vacancies, namely strontium vacancies, accompanied with either segregation of SrO impurity at the grain boundaries [41] or via formation of planar SrO defects similar to that in perovskite-related Ruddlesden–Popper (RP) structures [18,19]. The possibility of latter mechanism was confirmed directly by high-resolution electron microscopy [42–44] and was supported by computer simulation studies [44,45]. In present work, the microstructural studies did not reveal any impurity segregation in oxidized materials, thus supporting the second mechanism of charge compensation. The overall formula for prevailing trivalent praseodymium can be expressed, therefore, as $Sr_{1-1.5x}Pr_x^{3+}TiO_3*(SrO)_{0.5x}^{RP}$.

The defect chemistry may, thus, be described by reactions of formation of ionized strontium and oxygen vacancies in perovskite lattice (Eq. (2)) and oxygen exchange between the perovskite lattice and gas phase (Eq. (3)):

$$Sr_{Sr}^{\times} + O_O^{\times} \Leftrightarrow V_{Sr}'' + V_O^{\bullet\bullet} + SrO^{RP}, \quad K_1(T) = [V_{Sr}''][V_O^{\bullet\bullet}] \quad (2)$$

$$O_O^{\times} \Leftrightarrow V_O^{\bullet\bullet} + 2e + 0.5O_2, \quad K_2(T) = n^2 \times \delta \times p(O_2)^{1/2} \quad (3)$$

where $n = [Ti^{3+}]$. These mass action constants can be combined with the electroneutrality condition (Eq. (4)), on assuming that the concentration of electron holes remains negligible for donor-doped strontium titanate.
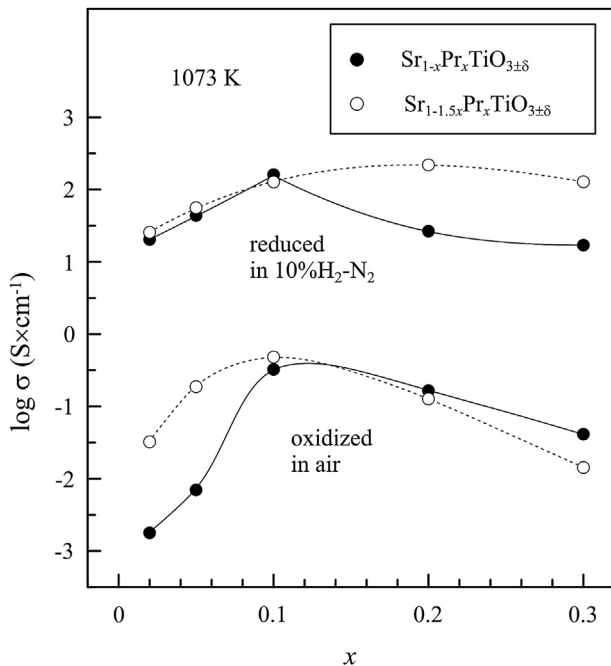
$$n + 2[V_{Sr}''] = 2[V_O^{\bullet\bullet}] + [Pr^{\bullet}] \quad (4)$$

The concentration of oxygen-ion vacancies should also remain negligible, at least under oxidizing conditions, when strontium vacancies are most likely to compensate the donor, yielding the approximate electroneutrality condition:

$$2[V_{Sr}''] \approx [Pr^{\bullet}] \quad (5)$$

Combining Eqs. (2), (3) and (5), electronic conductivity in Pr-substituted $SrTiO_3$ under oxidizing conditions can be expressed as

$$\sigma = e \times \mu \times n = e \times \mu \left(\frac{K_2}{2K_1}[Pr^{\bullet}]\right)^{0.5} p(O_2)^{-1/4} \quad (6)$$

where μ is the temperature-dependent electron mobility. Taking into account the XPS results, this defect chemistry mechanism is applicable for both $Sr_{1-x}Pr_xTiO_{3\pm\delta}$ and $Sr_{1-1.5x}Pr_xTiO_{3\pm\delta}$ series under oxidizing conditions, at least at high temperatures.

The electrical measurements at elevated temperature, 1573 K, showed that the conductivity of both cation-stoichiometric and A-site-deficient ceramics under oxidizing conditions increases with reducing oxygen partial pressure (Fig. 7A) and is proportional to
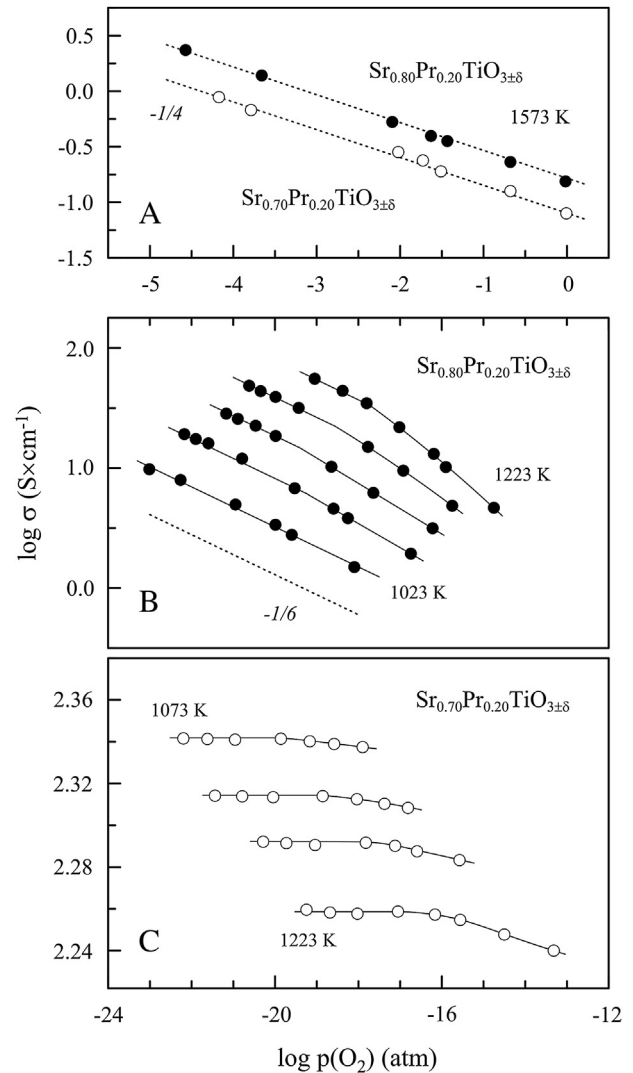

Fig. 7. Oxygen partial pressure dependencies of electrical conductivity of $Sr_{0.80}Pr_{0.20}TiO_{3\pm\delta}$ and $Sr_{0.70}Pr_{0.20}TiO_{3\pm\delta}$ ceramics under oxidizing (A) and reducing (B and C) conditions.

Fig. 6. Dependence of electrical conductivity of oxidized and reduced ceramics on praseodymium content at 1073 K.

$p(O_2)^{-1/4}$, as predicted by Eq. (6). One should note that oxygen exchange with the atmosphere is sluggish, even at high temperatures, and equilibration with gas phase at each $p(O_2)$ value took approximately 24 h at 1573 K. This is in agreement with literature reports indicating that equilibration in donor-doped titanates requires a long time, even at temperatures close to sintering conditions [19]. The defect equilibrium is nearly frozen at temperatures below 1473–1573 K, and thus the electrical properties are determined to significant extent by thermal pre-history.

Thermogravimetric studies in air showed very negligible variation of oxidized samples mass with temperature below 1300 K (Fig. 8). The estimations from TGA data showed that the changes in oxygen content between 573 and 1273 K did not exceed 0.003 oxygen atoms per formula unit. Similarly, the values of Seebeck coefficient showed only minor variation with temperature in the range 823–1223 K. Rough estimations of relative charge carrier concentration from Seebeck coefficient data using simplified Heikes formula (i.e. neglecting degeneracy factor and transported heat term) [46] yielded nearly temperature-independent values of n/N in the range 0.001–0.01. In the present case, the concentration of charge carries n can be considered equal to $[Ti^{3+}]$, and the density of state N equal to the total titanium content, although minor contribution of Pr^{3+}/Pr^{4+} couple to electronic transport process cannot be excluded. These estimates reflect also the level of oxygen nonstoichiometry in perovskite layers, as defined by reaction (4).

Thus, the thermogravimetric and thermopower data indicate that the charge carrier concentration in oxidized samples is nearly constant under the studied conditions, and the level of electrical conductivity is defined by their temperature-dependent mobility and donor dopant content. As expected (Eq. (6)), electrical

conductivity initially increases with praseodymium content reaching maximum at $x \approx 0.10-0.15$ (Fig. 6). Slow diminishing of electronic transport on further substitution can be ascribed to growing concentration of insulating planar RP-like defects, decreasing absolute concentration of mobile charge carriers per volume unit and limiting their mobility along z crystallographic axis.

3.4. Defect chemistry and electrical conductivity of reduced materials

Reduction or sintering under reducing conditions results in significant increase (2–3 orders of magnitude) of electronic conductivity compared to oxidized materials and transition to metallic-like behavior for most of compositions (Fig. 9). Concentration of n-type charge carriers (or Ti^{3+}) under this conditions should be determined by donor dopant content and oxygen deficiency in perovskite lattice; in simplest case (neglecting Pr^{4+} and other lattice defects) [19]:

$$n \approx 2[V_O^{\bullet\bullet}] + [Pr^{\bullet}] \tag{7}$$

For the $Sr_{1-x}Pr_xTiO_{3\pm\delta}$ series, one expects the following site occupancy:
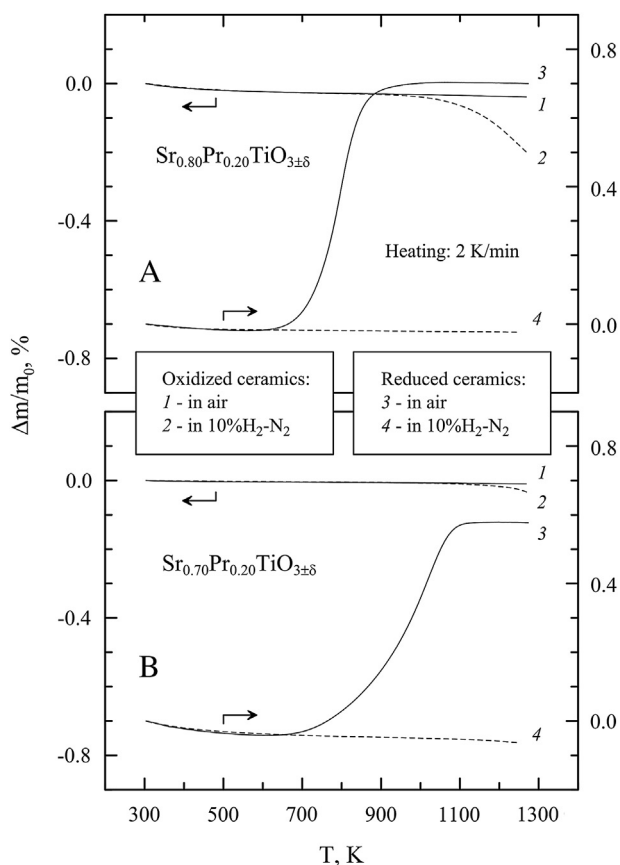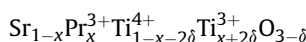
$$Sr_{1-x}Pr_x^{3+}Ti_{1-x-2\delta}^{4+}Ti_{x+2\delta}^{3+}O_{3-\delta}$$

Fig. 8. Relative weight change of oxidized and reduced powdered $Sr_{0.80}Pr_{0.20}TiO_{3\pm\delta}$ (A) and $Sr_{0.70}Pr_{0.20}TiO_{3\pm\delta}$ (B) samples on heating in different atmospheres.

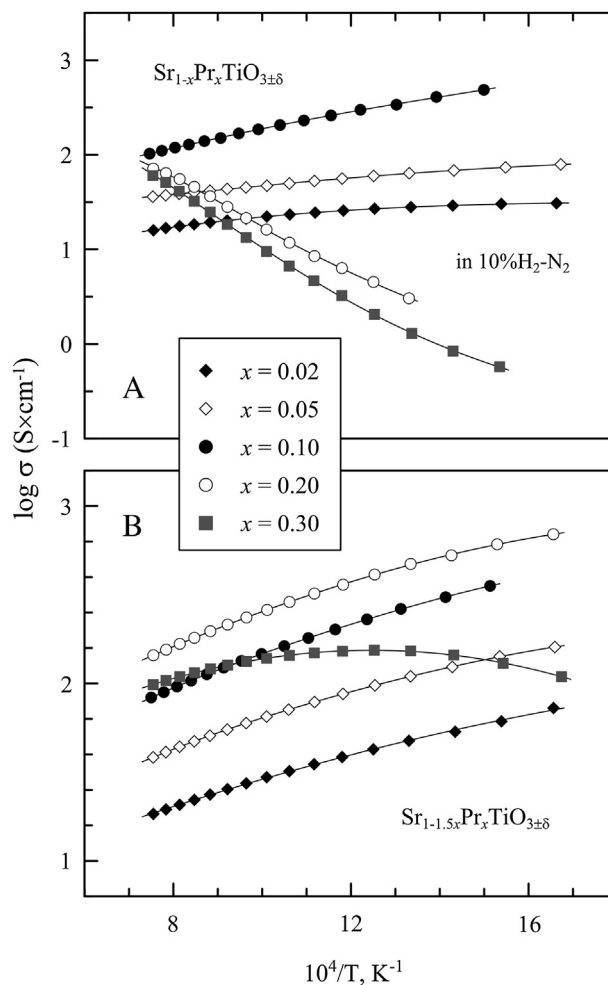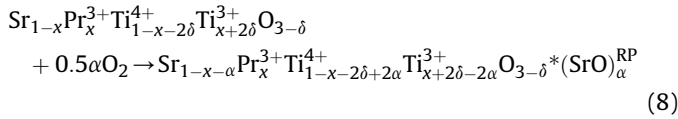**Fig. 9.** Temperature dependencies of electrical conductivity of (A) $Sr_{1-x}Pr_xTiO_{3\pm\delta}$ and (B) $Sr_{1-1.5x}Pr_xTiO_{3\pm\delta}$ ceramics in 10%H_2–N_2 atmosphere.

For significant donor dopant concentrations, however, the partial charge compensation via formation of Sr vacancies and RP defects (similar to oxidized materials) is not excluded; this gives:
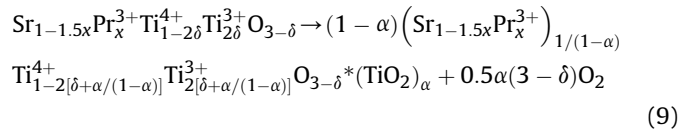
$$Sr_{1-x}Pr_x^{3+}Ti_{1-x-2\delta}^{4+}Ti_{x+2\delta}^{3+}O_{3-\delta}$$
$$+ 0.5\alpha O_2 \rightarrow Sr_{1-x-\alpha}Pr_x^{3+}Ti_{1-x-2\delta+2\alpha}^{4+}Ti_{x+2\delta-2\alpha}^{3+}O_{3-\delta}*(SrO)_\alpha^{RP} \quad (8)$$

Corresponding changes in oxygen stoichiometry for the limiting case $\alpha = x/2$ may account for up to 0.42% for $x = 0.1$, 0.82% for $x = 0.2$ and 1.20% for $x = 0.3$, even for negligible oxygen deficiency δ. Site occupancy may be close to $Sr_{1-x}Pr_x^{3+}Ti_{1-x-2\delta}^{4+}Ti_{x+2\delta}^{3+}O_{3-\delta}$ for very reduced samples, and is expected to evolve towards $Sr_{1-1.5x}Pr_x^{3+}Ti^{4+}O_3*(SrO)_{0.5x}^{RP}$ for oxidizing conditions.

Charge carrier concentration for $Sr_{1-1.5x}Pr_xTiO_{3\pm\delta}$ series in simplified case may be mainly determined by oxygen non-stoichiometry, combined with cation vacancies providing compensation for the donor species, with the following site occupancy:

$$Sr_{1-1.5x}Pr_x^{3+}Ti_{1-2\delta}^{4+}Ti_{2\delta}^{3+}O_{3-\delta}$$
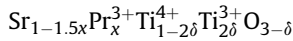
However, the perovskite structure may not allow incorporation of excessive fractions of cation vacancies, mainly for the highest contents of praseodymium, thus forcing segregation of titanium excess. In this case:

$$Sr_{1-1.5x}Pr_x^{3+}Ti_{1-2\delta}^{4+}Ti_{2\delta}^{3+}O_{3-\delta} \rightarrow (1-\alpha)\left(Sr_{1-1.5x}Pr_x^{3+}\right)_{1/(1-\alpha)}$$
$$Ti_{1-2[\delta+\alpha/(1-\alpha)]}^{4+}Ti_{2[\delta+\alpha/(1-\alpha)]}^{3+}O_{3-\delta}*(TiO_2)_\alpha + 0.5\alpha(3-\delta)O_2 \quad (9)$$

where "TiO$_2$" is either TiO$_2$ Magneli double layers embedded into the SrTiO$_3$ perovskite matrix or precipitated Ti$_n$O$_{2n-1}$ Magneli phases [14,18]. Note that onset of titania-rich precipitates were also reported for other donor-doped strontium titanate materials, upon changing from oxidizing to reducing conditions [17].

In order to estimate oxygen content in reduced materials, powdered reduced ceramics were oxidized in air in the course of TGA experiment (Fig. 10B and C). The mass change during oxidation was found to increase continuously with increasing praseodymium content. Fig. 11 shows calculated overall oxygen nonstoichiometry in reduced materials assuming that after oxidation $[Ti^{3+}] \rightarrow 0$, and that praseodymium is either only in 3+ state or co-exists in 3+ and 4+ states in similar contents ($[Pr^{4+}]/[Pr^{3+}] = 1:1$). The filled areas in Fig. 11 correspond respectively to intermediate Pr^{4+} fractions in oxidized materials. These estimations suggest that all reduced $Sr_{1-x}Pr_xTiO_{3\pm\delta}$ ceramics show overall oxygen excess (if one considers the nominal composition as a reference), while $Sr_{1-1.5x}Pr_xTiO_{3\pm\delta}$ are characterized, as expected, with oxygen deficiency. Taking into account the XPS results (Table 4), the true values should be close to the upper border of marked areas in Fig. 11. The only exception from the observed dependencies is $Sr_{0.55}Pr_{0.30}TiO_{3\pm\delta}$ (Figs. 10C and 11B), most likely, due to noticeable amount of impurity observed by SEM.

Thus, the TGA results lead to conclusion that for all $Sr_{1-x}Pr_xTiO_{3\pm\delta}$ reduced ceramics the defect chemistry is realized via complex site occupancy, $Sr_{1-x-\alpha}Pr_x^{3+}Ti_{1-x-2\delta+2\alpha}^{4+}Ti_{x+2\delta-2\alpha}^{3+}O_{3-\delta}*(SrO)_\alpha^{RP}$, combining A-site vacancies and electronic defects. Fig. 11A (right Y axis) shows estimated oxygen deficiency δ in perovskite matrix assuming the limiting case of $\alpha = x/2$. Site occupancy is expected to be close to nominal composition for $Sr_{1-1.5x}Pr_xTiO_{3-\delta}$ ($x = 0.02-0.10$), while microstructural studies indicate more complex charge compensation and site-occupancy for reduced $Sr_{0.70}Pr_{0.20}TiO_{3\pm\delta}$ and $Sr_{0.55}Pr_{0.30}TiO_{3\pm\delta}$ with
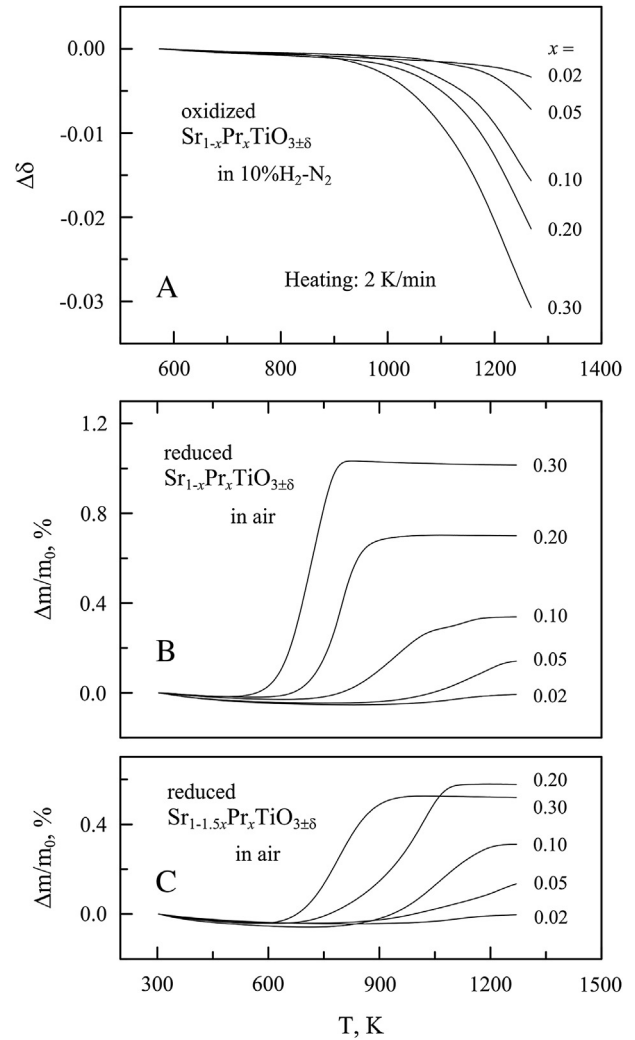
Fig. 10. Relative weight change of oxidized powdered $Sr_{1-x}Pr_xTiO_{3\pm\delta}$ samples on heating in 10%H$_2$–N$_2$ flow, and reduced $Sr_{1-x}Pr_xTiO_{3\pm\delta}$ (B) and $Sr_{1-1.5x}Pr_xTiO_{3\pm\delta}$ (C) samples on heating in air.

precipitation of Ti-rich phase, as described by Eq. (9). Once again, one should mention that in all cases the charge compensation should be even more complex due to the presence of Pr^{4+} as indicated by XPS analysis (Table 4).

As expected (Eq. (7)), electrical conductivity initially increases with Pr substitution (Figs. 6 and 9) and is on the same level for both $Sr_{1-x}Pr_xTiO_{3\pm\delta}$ and $Sr_{1-1.5x}Pr_xTiO_{3\pm\delta}$ ($x = 0.02-0.10$). For $Sr_{1-1.5x}Pr_xTiO_{3\pm\delta}$ series, the maximum conductivity is characteristic for $x = 0.20$; decrease of electronic transport is observed on further substitution, most likely, due to non-negligible TiO$_2$ segregation and deviation from nominal composition in the major phase. Somewhat different behavior was found for $Sr_{1-x}Pr_xTiO_{3\pm\delta}$ series, with drop of conductivity for $Sr_{0.80}Pr_{0.20}TiO_{3\pm\delta}$ and $Sr_{0.70}Pr_{0.30}TiO_{3\pm\delta}$ ceramics. Furthermore, contrary to other compositions, these two materials exhibited semiconducting behavior in the studied temperature range, 550–1300 K. Note that the thermogravimetric studies confirmed very negligible weight variation on heating/cooling in 10%H$_2$–N$_2$ atmosphere (i.e. under conditions corresponding to conductivity vs. T measurements) for all powdered ceramics (Fig. 8), thus suggesting very negligible oxygen nonstoichiometry changes under these conditions.

The difference in electrical behavior of $Sr_{1-x}Pr_xTiO_{3\pm\delta}$ ($x = 0.20-0.30$) can be explained by two main reasons. Firstly, increasing
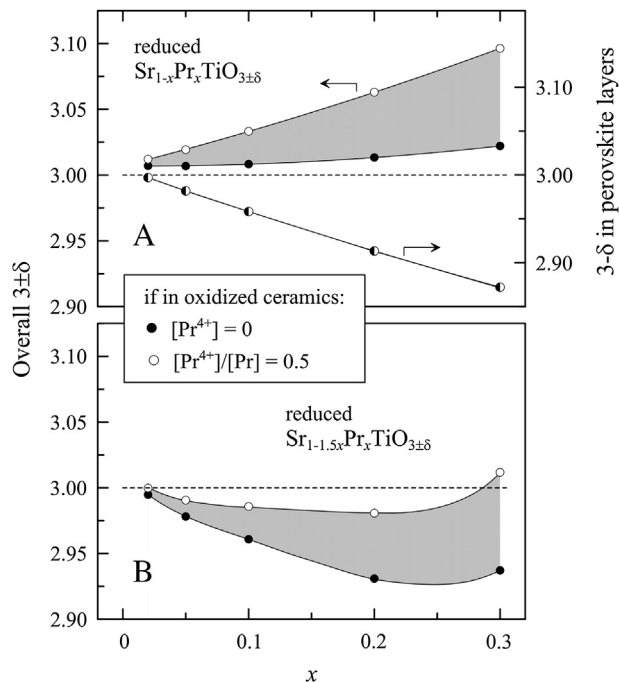
Fig. 11. Overall oxygen nonstoichiometry in reduced $Sr_{1-x}Pr_xTiO_{3\pm\delta}$ (A) and $Sr_{1-1.5x}Pr_xTiO_{3\pm\delta}$ (B) ceramics estimated from the thermogravimetric data (Fig. 10B and C) assuming that either all Pr in oxidized samples is in 3+ oxidation state or $[Pr^{4+}]/[Pr] = 0.5$. Filled areas correspond to intermediate Pr^{4+} fractions. The curve with semi-filled symbols (right Y axis) corresponds to estimated values of oxygen deficiency in perovskite matrix for limiting case of $\alpha = x/2$ (see text).

praseodymium content in "cation-stoichiometric" compositions leads to increase of insulating RP-like planar defects, which may induce localization of electronic charge carriers and, consequently, thermally-activated conductivity. This is contrary to other composition, where n-type charge carriers are delocalized and metallic-like conduction is observed in the studied temperature range. Secondly, contrary to other reduced ceramics, $Sr_{1-x}Pr_xTiO_{3\pm\delta}$ ($x = 0.20-0.30$) samples showed relatively high porosity (Table 1). As mentioned above, the equilibrium in cation sublattice in donor-doped titanates can be achieved only at high temperatures, while below ~ 1473 K cation defect distribution is kinetically nearly frozen. Significant porosity may promote oxygen exchange with the atmosphere thus facilitating equilibration with gas phase and cation defect redistribution at sintering temperatures and on subsequent cooling in temperature range 1273–1773 K; this may yield different defect distribution at low temperatures in porous and dense materials.

The difference in defect chemistry under similar conditions is also reflected by observed $p(O_2)$-dependencies of electrical conductivity (Fig. 7B and C). Electronic transport in materials with semiconducting behavior increases on reducing oxygen partial pressure. The charge carrier concentration is governed by equilibrium with gas phase, Eq. (3), and simplified electroneutrality condition is given by (oxygen vacancy compensation):

$$n \approx 2[V_O^{\bullet\bullet}] \tag{10}$$

In combination with Eq. (3), this yields $\sigma \sim p(O_2)^{-1/6}$ dependencies, in agreement with experimental data (Fig. 7B). In $(Sr,Pr)TiO_{3\pm\delta}$ ceramics with metallic-like conductivity, the charge carrier concentration below 1273 K is determined by frozen cation defects equilibrium, and electroneutrality conditions can be expressed by (prevailing donor compensation):

$$n \approx [D^{\bullet}]^{eff} = [Pr^{\bullet}] + 2[Pr^{\bullet\bullet}] - 2[V_{Sr}''] \tag{11}$$

where $[D^{\bullet}]^{eff}$ is effective donor concentration [20], after subtracting the acceptor-type contribution of A-site vacancies. As a result, the conductivity shows nearly $p(O_2)$-independent behavior under studied conditions (Fig. 7C).

3.5. Redox behavior

In-situ reduction of anode layers was simulated by monitoring the conductivity relaxation of selected $(Sr,Pr)TiO_{3\pm\delta}$ during reduction–oxidation cycles at 1173 K (Fig. 12). The first experiments were conducted using dense oxidized samples (Fig. 12A and D). The results showed very slow increase of conductivity on reduction and slow decrease on subsequent oxidation. After ~ 50 h of reduction at this temperature, the conductivity was still ~ 1.5 order of magnitude lower compared to the ceramic samples reduced at high temperatures. Furthermore, the shape of the relaxation curves indicates that the expected high level of conductivity cannot be reached in reasonable time span.

As oxidized materials are characterized with very low concentration of oxygen vacancies, and, therefore, reduction could be limited by slow oxygen diffusion out of the bulk of dense ceramics, further experiments were performed using the porous samples
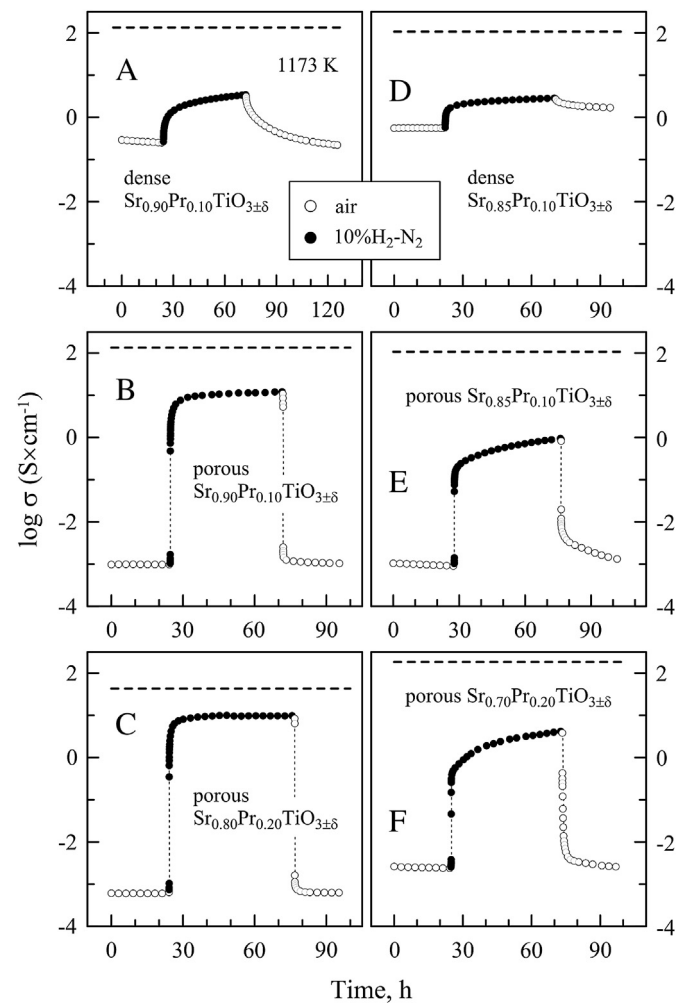
Fig. 12. Electrical conductivity relaxation on reduction and subsequent re-oxidation of dense and porous oxidized $Sr_{1-x}Pr_xTiO_{3\pm\delta}$ (A–C) and $Sr_{1-1.5x}Pr_xTiO_{3\pm\delta}$ (D–F) ceramic samples at 1173 K. Thick dotted line corresponds to the conductivity of dense ceramics sintered under reducing conditions at high temperature.

(Table 1) with increased gas/solid interface area in order to improve oxygen exchange and facilitate the reduction. Porous $Sr_{1-x}Pr_xTiO_{3\pm\delta}$ ceramics indeed showed faster re-equilibration and conductivity relaxation in redox cycles (Fig. 12B and C). Also, despite a significant porosity, the conductivity values after reduction were higher if compared to dense samples with the same composition after the same treatment (Fig. 12A and B). Still, the level of conductivity was around order of magnitude lower than expected. Correction for porosity may give only slightly higher ($\sim$twofold) conductivity values. "Cation-deficient" $Sr_{1-1.5x}Pr_xTiO_{3\pm\delta}$ ceramic samples even with porous morphology exhibited much slower kinetics of reduction and lower conductivity level (Fig. 12E and F).

The results of thermogravimetric measurements correlated with the conductivity relaxation data. Firstly, the relative weight change and, consequently, oxygen content variations in $Sr_{1-1.5x}Pr_xTiO_{3\pm\delta}$ during reduction on heating in hydrogen-containing atmospheres are much smaller compared to "cation-stoichiometric" compositions (Fig. 8). Furthermore, oxygen content changes upon reduction in heating regime showed direct correlation with praseodymium substitution level in $Sr_{1-x}Pr_xTiO_{3\pm\delta}$ series (Fig. 8); no evident compositional dependence was found for "cation-deficient" materials. In addition, isothermal experiments confirmed that $Sr_{1-x}Pr_xTiO_{3\pm\delta}$ ceramics undergo much faster and deeper reduction compared to $Sr_{1-1.5x}Pr_xTiO_{3\pm\delta}$ counterparts (Fig. 13); "cation-stoichiometric" samples seem to tend to constant weight after $\sim$30 h of reduction.
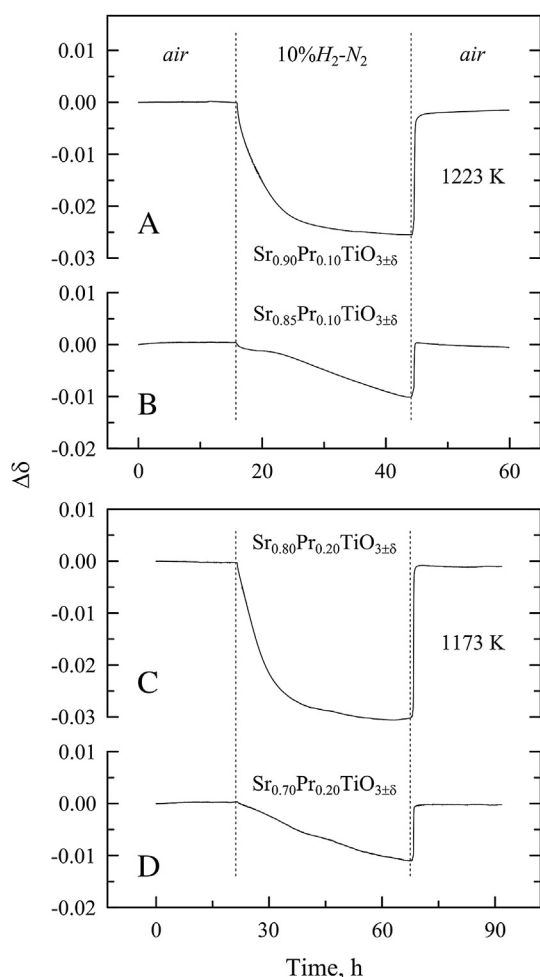

Fig. 13. Relative weight variations of oxidized powdered $(Sr,Pr)TiO_{3\pm\delta}$ ceramic samples on reduction and subsequent re-oxidation at (A,B) 1223 K and (C,D) 1173 K.

Taking into account the defect chemistry discussed above, the changes in crystal lattice induced by reduction should be quite similar for most studied materials. This should include partial or complete dissolution of RP-like SrO defects in the perovskite matrix, possibly combined with formation of oxygen vacancies via oxygen release from the lattice. For $Sr_{1-1.5x}Pr_xTiO_{3\pm\delta}$ ($x = 0.20–0.30$), the reduction process may also include a segregation of TiO_2-based impurities. Thus, the overall reduction process should involve conjugate reconstruction of cation sublattice and re-equilibration of oxygen sublattice with gas phase. However, as mentioned above, the equilibrium in cation sublattice is nearly frozen at temperatures below $\sim$1473 K. Strontium vacancy diffusion was shown to be predominant mechanism of cation sublattice re-equilibration [47,48] and is the limiting step of overall reduction process for donor-doped titanates. For instance, even at 1523–1773 K, cation diffusion in donor-doped $SrTiO_3$ single crystals was reported to be several orders of magnitude slower that the oxygen diffusion [48]. At the same time, re-equilibration in oxygen sublattice on reduction at $\leq$1173 K may be also stagnated due to very low concentration of oxygen vacancies, at least in oxidized materials. Oxygen-tracer diffusion experiments on lanthanum-doped $SrTiO_3$ single crystals have found very low diffusion coefficients at 973–1173 K, between 2×10^{-15} and 10^{-13} cm^2 s^{-1} [49]. Note that the corresponding range of spatial scale for diffusion controlled processes ($\approx 2(Dt)^{1/2}$) is about 0.2–1.2 μm within the time scale of 10 h; this indicates that redox kinetics may be affected by sluggish diffusion even at grain size scale.

As the reduction mechanism should be common for both $Sr_{1-x}Pr_xTiO_{3\pm\delta}$ and $Sr_{1-1.5x}Pr_xTiO_{3\pm\delta}$ series, the difference in behavior observed by TGA and conductivity relaxation experiments can be attributed mainly to microstructural features. It was suggested earlier for polycrystalline La- and Y-doped $SrTiO_3$ [11,13] that the reduction process involves relatively fast initial reduction of grain surfaces/grain boundaries followed by slow diffusion of oxygen vacancies into the grain bulk. Similar mechanism can be expected for praseodymium-substituted materials. At the same time, $Sr_{1-1.5x}Pr_xTiO_{3\pm\delta}$ compositions are characterized with much larger average grain size compared to "cation-stoichiometric" ceramics, and porous $Sr_{1-1.5x}Pr_xTiO_{3\pm\delta}$ ceramic samples used for conductivity measurements showed smaller porosity despite lower sintering temperatures (Table 1). Thus, significantly larger surface/grain boundary area, combined with gas phase diffusion in porous ceramics, ensure faster reduction kinetics for $Sr_{1-x}Pr_xTiO_{3\pm\delta}$ ceramic materials. One should note that the role of oxygen vacancy concentration in kinetics of redox processes is confirmed also by fast re-oxidation of reduced samples in both thermogravimetric and conductivity relaxation experiments (Figs. 10, 12 and 13). Still, it is not clear if the complete reduction and, therefore, high level of electrical conductivity can be achieved even for nanocrystalline powders and electrode layers by in-situ treatment at temperatures of $\approx$1173 K.

3.6. Thermal and chemical expansion

Dilatometric studies showed that all oxidized and reduced $(Sr,Pr)TiO_{3\pm\delta}$ ceramic materials exhibit nearly linear thermal expansion in corresponding atmospheres (Fig. 14). Thermogravimetric results (Fig. 8) confirmed that oxygen nonstoichiometry variations are negligible on heating/cooling in fixed-composition atmospheres; therefore, the chemical contribution to thermal expansion can be excluded under these conditions. Reduction results only in a minor increase of thermal expansion (Fig. 14B), and average thermal expansion coefficients (TECs) vary in the narrow range (11.3–12.6) $\times$ 10^{-6} K^{-1} for both reduced and oxidized ceramics (Table 5). These moderate TEC values ensure thermo-mechanical compatibility of $(Sr,Pr)TiO_{3\pm\delta}$ electrode layers with
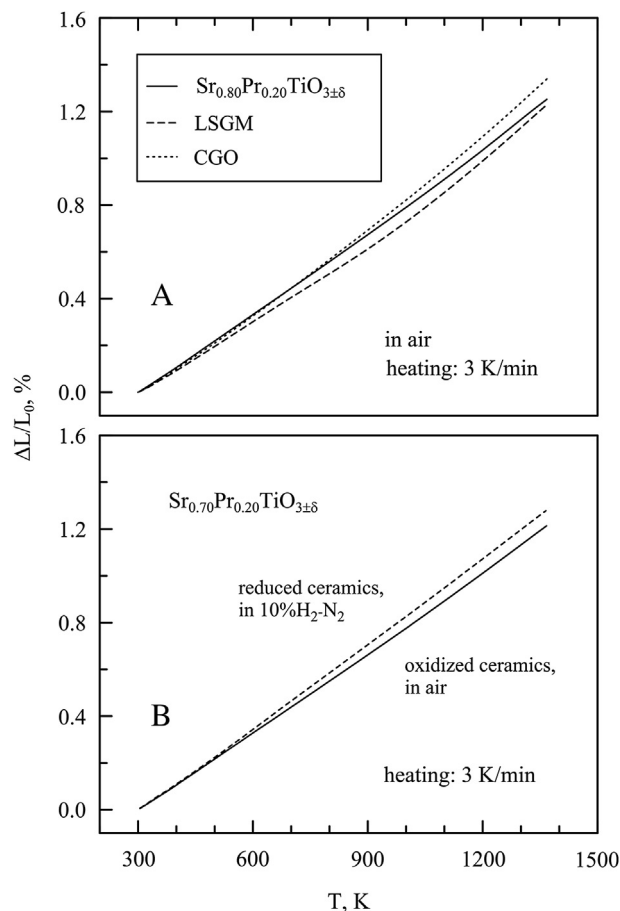
**Fig. 14.** Dilatometric curves of (A) oxidized $Sr_{0.80}Pr_{0.20}TiO_{3\pm\delta}$ ceramics in air in comparison with LSGM and CGO solid electrolytes, and (B) oxidized and reduced $Sr_{0.70}Pr_{0.20}TiO_{3\pm\delta}$ ceramics in corresponding atmospheres.

common solid electrolytes such as CGO or LSGM (Fig. 14A and Table 5), as well as with yttria-stabilized zirconia or lanthanum silicate-based apatite-type solid electrolytes.

Fig. 15 illustrates the isothermal dimensional changes for selected $(Sr,Pr)TiO_{3\pm\delta}$ ceramics upon reduction at 1223 K. Only porous ceramic samples (Table 1) were used for these experiments to ensure faster equilibration with gas atmosphere. The changes of oxidation state and, correspondingly, changes in ionic radii of variable-valence cations titanium cations $(r_{Ti^{3+}} > r_{Ti^{4+}})$ and/or praseodymium cations $(r_{Pr^{3+}} > r_{Pr^{4+}})$ as well as reconstruction of cation sublattice induced by reduction may result in dimensional

Table 5
Average thermal expansion coefficients of $(Sr,Pr)TiO_{3\pm\delta}$ ceramics at 300–1373 K.

Composition	$(\overline{\alpha} \times 10^6) \pm 0.1$, K^{-1}	
	Oxidized ceramics, in air	Reduced ceramics, in 10%H$_2$−N$_2$
$Sr_{0.98}Pr_{0.02}TiO_{3\pm\delta}$	11.6	11.7
$Sr_{0.95}Pr_{0.05}TiO_{3\pm\delta}$	11.5	11.9
$Sr_{0.90}Pr_{0.10}TiO_{3\pm\delta}$	11.6	11.9
$Sr_{0.80}Pr_{0.20}TiO_{3\pm\delta}$	11.7	12.3
$Sr_{0.70}Pr_{0.30}TiO_{3\pm\delta}$	11.9	12.6
$Sr_{0.97}Pr_{0.02}TiO_{3\pm\delta}$	11.5	11.7
$Sr_{0.925}Pr_{0.05}TiO_{3\pm\delta}$	11.5	11.7
$Sr_{0.85}Pr_{0.10}TiO_{3\pm\delta}$	11.5	11.9
$Sr_{0.70}Pr_{0.20}TiO_{3\pm\delta}$	11.4	12.1
$Sr_{0.55}Pr_{0.30}TiO_{3\pm\delta}$	11.3	12.1
CGO	12.6	
LSGM	11.3	
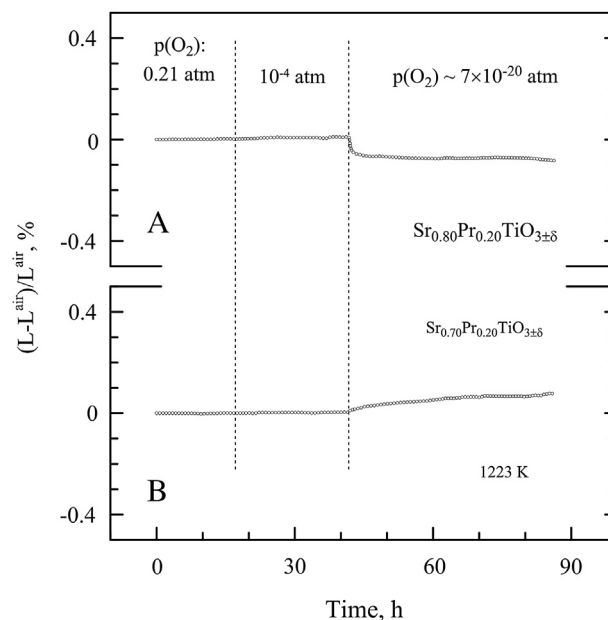
Fig. 15. Relative length changes of oxidized $Sr_{0.80}Pr_{0.20}TiO_{3\pm\delta}$ (A) and $Sr_{0.70}Pr_{0.20}TiO_{3\pm\delta}$ (B) ceramics on reduction at 1223 K.

changes in ceramics materials (so called chemical strain or expansion/contraction). The rate of dimensional changes due to reduction was found to be in good agreement with the thermogravimetric observations. While relatively fast apparent equilibration was found for $Sr_{1-x}Pr_xTiO_{3\pm\delta}$ ceramics (Fig. 15A), the length of $Sr_{1-1.5x}Pr_xTiO_{3\pm\delta}$ samples slowly drifted with time (Fig. 15B). The values of chemical strain of ceramic samples at 1223 K due to reduction are summarized in Table 6. "A-site deficient" samples showed minor expansion increasing with praseodymium substitution and mainly associated with increasing concentration of oxygen vacancies in perovskite lattice. Unusually, $Sr_{1-x}Pr_xTiO_{3\pm\delta}$ ceramic samples exhibited quantitatively similar contraction upon reduction. This kind of behavior may serve as additional indication of specific defect chemistry of donor-doped titanates and presence of RP-like planar defects in crystal lattice. In particular, decreasing oxygen content in RP-type $La_2NiO_{4+\delta}$-based materials on reducing $p(O_2)$ was found to results in expansion along ab crystallographic plane and contraction along c axis [50]. Apparently, similar effects are characteristic for $Sr_{1-x}Pr_xTiO_{3\pm\delta}$ materials.

Whatever the mechanism of chemical-induced expansion/contraction in substituted SrTiO$_3$, isothermal dilatometric studies indicate favorably small dimensional changes in Pr-substituted materials. Rather negligible chemical strain should provide dimensional stability of electrode layers upon in-situ reduction in solid electrolyte cell, in the course of redox cycles, and under polarization-induced oxygen chemical potential gradient. In addition, chemical expansion/contraction of $(Sr,Pr)TiO_{3\pm\delta}$ was found to be noticeably smaller compared to other alternative anode materials such as perovskite-like $(La,Sr)(Mn,B)O_{3-\delta}$ (Fig. 16), thus making them preferable for this application from thermomechanical stability point of view.

Table 6
Isothermal dimensional changes of $(Sr,Pr)TiO_{3\pm\delta}$ ceramics on reduction at 1223 K.

Composition	$p(O_2)$ in reducing atmosphere, atm	$(L - L^{air})/L^{air}$, %
$Sr_{0.90}Pr_{0.10}TiO_{3\pm\delta}$	4×10^{-20}	−0.014
$Sr_{0.80}Pr_{0.20}TiO_{3\pm\delta}$	9×10^{-20}	−0.076
$Sr_{0.85}Pr_{0.10}TiO_{3\pm\delta}$	4×10^{-20}	0.025
$Sr_{0.70}Pr_{0.20}TiO_{3\pm\delta}$	5×10^{-20}	0.077
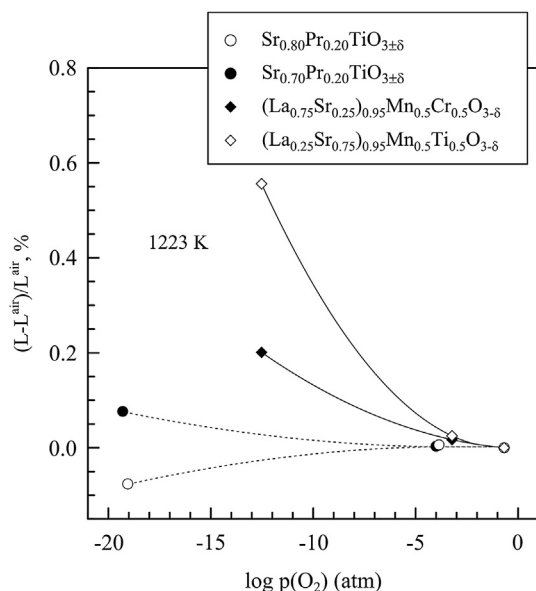
Fig. 16. Chemical strain of $(Sr,Pr)TiO_{3\pm\delta}$ ceramics with respect to atmospheric oxygen pressure. Literature data on $(La,Sr)(Mn,B)O_{3-\delta}$ (B = Cr and Ti) perovskites [51] ate shown for comparison.

4. Conclusions

(i) Formation of $Sr_{1-x}Pr_xTiO_{3\pm\delta}$ and $Sr_{1-1.5x}Pr_xTiO_{3\pm\delta}$ ($x = 0.02$–0.30) single-phase ceramic materials with perovskite-like structure under both oxidizing and reducing conditions was confirmed by XRD analysis, while microstructural studies indicated minor segregation of TiO_2 impurity for reduced $Sr_{0.70}Pr_{0.20}TiO_{3\pm\delta}$ and $Sr_{0.55}Pr_{0.30}TiO_{3\pm\delta}$;

(ii) Praseodymium cations were found to substitute into strontium sublattice in mixed 4+/3+ oxidation state ($\sim$1:1 ratio) and are essentially insoluble in titanium sublattice under applied conditions;

(iii) All oxidized materials exhibit oxygen excess correlated with praseodymium content. Under reducing conditions, $Sr_{1-x}Pr_xTiO_{3\pm\delta}$ solid solutions retain overall oxygen over stoichiometry, while $Sr_{1-1.5x}Pr_xTiO_{3\pm\delta}$ are characterized with minor oxygen deficiency;

(iv) High-temperature reduction under reducing conditions results in 2–3 orders of magnitude increase of n-type electronic conductivity with respect to oxidized materials. Electrical properties were discussed in conjunction with defect chemistry of donor-doped $SrTiO_3$;

(v) Thermogravimetric and electrical studies demonstrated very slow kinetics of reduction at 1173 K associated mainly with nearly frozen equilibrium in cation sublattice at this temperature and which may limit the level of electronic conductivity in in-situ reduced anodes;

(vi) All studied materials exhibit moderate, almost $p(O_2)$-independent thermal expansion coefficients, which ensure the compatibility with common solid electrolytes, and favorably small chemical strain on reducing oxygen partial pressure.

References

[1] D. Sarantaridis, A. Atkinson, Fuel Cells 7 (2007) 246–258.
[2] Y. Matsuzaki, I. Yasuda, Solid State Ionics 132 (2000) 261–269.
[3] J.W. Fergus, Solid State Ionics 177 (2006) 1529–1541.
[4] A. Orera, P.R. Slater, Chem. Mater. 22 (2010) 675–690.
[5] D.J. Cumming, V.V. Kharton, A.A. Yaremchenko, A.V. Kovalevsky, J.A. Kilner, J. Am. Ceram. Soc. 94 (2011) 2993–3000.
[6] J.C. Ruiz-Morales, J. Canales-Vazquez, C. Savaniu, D. Marrero-Lopez, P. Nunez, W. Zhou, J.T.S. Irvine, Phys. Chem. Chem. Phys. 9 (2007) 1821–1830.
[7] H. Kurokawa, L. Yang, C.P. Jacobson, L.C. De Jonghe, S.J. Visco, J. Power Sources 164 (2007) 510–518.
[8] R. Mukundan, E.L. Brosha, F.H. Garzon, Electrochem. Solid-State Lett. 7 (2004) A5–A7.
[9] C.D. Savaniu, J.T.S. Irvine, J. Mater. Chem. 19 (2009) 8119–8128.
[10] O.A. Marina, N.L. Canfield, J.W. Stevenson, Solid State Ionics 149 (2002) 21–28.
[11] D. Neagu, J.T.S. Irvine, Chem. Mater. 22 (2010) 5042–5053.
[12] X. Li, H. Zhao, W. Shen, F. Gao, X. Huang, Y. Li, Z. Zhu, J. Power Sources 166 (2007) 47–52.
[13] S. Hui, A. Petric, J. Eur. Ceram. Soc. 22 (2002) 1673–1681.
[14] T. Kolodiazhnyi, A. Petric, J. Electroceram. 15 (2005) 5–11.
[15] A.M. Hussain, J.V.T. Hgh, W. Zhang, N. Bonanos, J. Power Sources 216 (2012) 308–313.
[16] A.M. Hussain, J.V.T. Hgh, T. Jacobsen, N. Bonanos, Int. J. Hydrogen Energy 37 (2012) 4309–4318.
[17] P. Blennow, K.K. Hansen, L.R. Wallenberg, M. Mogensen, ECS Trans. 13 (2008) 181–194.
[18] P. Blennow, A. Hagen, K.K. Hansen, L.R. Wallenberg, M. Mogensen, Solid State Ionics 179 (2008) 2047–2058.
[19] R. Moos, K.H. Hardtl, J. Am. Ceram. Soc. 80 (1997) 2549–2562.
[20] R. Meyer, R. Waser, Sens. Actuators B 101 (2004) 335–345.
[21] A. Duran, E. Martinez, J.A. Diaz, J.M. Siqueiros, J. Appl. Phys. 97 (2005) 104109.
[22] A. Duran, E. Martinez, J.M. Siqueiros, Integr. Ferroelectr. 71 (2005) 115–120.
[23] A. Duran, F. Morales, L. Fuentes, J.M. Siqueiros, J. Phys. Condens. Matter 20 (2008) 085219.
[24] R. Garg, A. Senyshyn, H. Boysen, R. Ranjan, Phys. Rev. B 79 (2009) 144122.
[25] I.A. Sluchinskaya, A.I. Lebedev, A. Erko, J. Appl. Phys. 112 (2012) 024103.
[26] X. Wang, Q. Hu, L. Li, X. Lu, J. Appl. Phys. 112 (2012) 044106.
[27] E.V. Tsipis, V.V. Kharton, J. Solid State Electrochem 12 (2008) 1367–1391.
[28] J.H. Scofield, J. Electron. Spectrosc. 8 (1976) 129–137.
[29] F.W. Lytle, J. Appl. Phys. 35 (1964) 2212–2215.
[30] A. Okazaki, M. Kawaminami, Mater. Res. Bull. 8 (1973) 545–550.
[31] M. Mori, K. Nakamura, T. Itoh, J. Fuel Cell Sci. Technol. 9 (2012) 021007.
[32] S. Ltkehoff, M. Neumann, Phys. Rev. B 52 (1995) 13808–13811.
[33] A. Schaefer, S. Gevers, V. Zielasek, T. Schroeder, J. Falta, J. Wollschlager, M. Bumer, J. Chem. Phys. 134 (2011) 054701.
[34] A. Bianconi, A. Kotani, K. Okada, A. Marcelli, T. Miyahara, Phys. Rev. B 38 (1988) 3433–3437.
[35] J.F. Moulder, W.F. Stickle, P.E. Sobol, K.D. Bomben, Handbook of X-ray Photoelectron Spectroscopy, Physical Electronics, Minnesota, USA, 1995.
[36] M.Y. Sinev, G.W. Graham, L.P. Haack, M. Shelef, J. Mater. Res. 11 (1996) 1960–1970.
[37] H. Ogasawara, A. Kotani, B.T. Thole, Phys. Rev. B 44 (1991) 5465–5469.
[38] I. Luciu, R. Bartali, N. Laidani, J. Phys. D Appl. Phys. 45 (2012) 345302.
[39] H. Borchert, Y.V. Frolova, V.V. Kaichev, I.P. Prosvirin, G.M. Alikina, A.I. Lukashevich, V.I. Zaikovskii, E.M. Moroz, S.N. Trukhan, V.P. Ivanov, E.A. Paukshtis, V.I. Bukhtiyarov, V.A. Sadykov, J. Phys. Chem. B 109 (2005) 5728–5738.
[40] N.H. Chan, R.K. Sharma, D.M. Smyth, J. Electrochem. Soc. 128 (1981) 1762–1769.
[41] R. Meyer, R. Waser, J. Helmbold, G. Borchardt, J. Electroceram. 9 (2002) 101–110.
[42] R.J.D. Tilley, J. Solid State Chem. 21 (1977) 293–301.
[43] A. Ovalle, J.C. Ruiz-Morales, J. Canales-Vazquez, D. Marrero-Lopez, J.T.S. Irvine, Solid State Ionics 177 (2006) 1997–2003.
[44] M.A. McCoy, R.W. Grimes, W.E. Lee, Philos. Mag. 75 (1997) 833–846.
[45] M.J. Akhtar, Z.U.N. Akhtar, R.A. Jackson, C.R.A. Catlow, J. Am. Ceram. Soc. 78 (1995) 421–428.
[46] K. Kobayashi, S. Yamaguchi, M. Mukaida, T. Tsunoda, Solid State Ionics 144 (2001) 315–320.
[47] R. Meyer, R. Waser, J. Helmbold, G. Borchardt, Phys. Rev. Lett. 90 (2003) 105901.
[48] K. Gomann, G. Borchardt, M. Schulz, A. Gmann, W. Maus-Friedrichs, B. Lesage, O. Katasov, S. Hoffmann-Eifert, T. Schneller, Phys. Chem. Chem. Phys. 7 (2005) 2053–2060.
[49] U. Kiessling, J. Claus, G. Borchardt, S. Weber, S. Scherrer, J. Am. Ceram. Soc. 77 (1994) 2188–2190.
[50] V.V. Kharton, A.V. Kovalevsky, M. Avdeev, E.V. Tsipis, M.V. Patrakeev, A.A. Yaremchenko, E.N. Naumovich, J.R. Frade, Chem. Mater. 19 (2007) 2027–2033.
[51] V.A. Kolotygin, E.V. Tsipis, A.L. Shaula, E.N. Naumovich, J.R. Frade, S.I. Bredikhin, V.V. Kharton, J. Solid State Chem. 15 (2011) 313–327.